FDTD Analysis of Microwave Hearing Effect

Yoshiaki Watanabe, Toshiyuki Tanaka, *Member, IEEE*, Masao Taki, and So-ichi Watanabe, *Member, IEEE*

***Abstract*—This paper presents a numerical analysis of the thermoelastic waves excited by the absorbed energy of pulsed microwaves in a human head. First, we calculate the distribution of the specific absorption rate using a conventional finite-difference time-domain (FDTD) algorithm for the Maxwell's equation. We then calculate the elastic waves excited by the absorbed microwave energy. The FDTD method is again applied to solve the elastic-wave equations. The validity of the analysis for elastic waves is confirmed through comparison of the FDTD results with the analytical solutions in a sphere model. Two anatomically based human head models are employed for numerical calculations. The waveforms of the calculated pressure waves are different from the previously reported ones. It is especially shown that the surface heating is important in exciting the fundamental mode of the pressure waves in the head. The pulsewidth dependency of the loudness of microwave hearing is clearly explained by the simulation with realistic head models. The peak pressure of elastic waves in the realistic head models is of the same order as the previously reported values obtained with a homogeneous sphere model. The strength of elastic wave is discussed in consideration of the safety of this phenomenon.**

***Index Terms*—Microwave hearing, microwave auditory effect, FDTD methods, thermoelasticity.**

I. Introduction

OVER 20 YEARS, a considerable number of studies have been made on the microwave auditory effect, or microwave hearing effect, which is an effect of auditory sensations produced by appropriately modulated microwaves [1]–[13]. Thermoelastic expansion has been proposed as a hypothesis for the mechanism of this phenomenon. The absorbed energy of pulsed microwaves produce small, but rapid temperature rise in the tissue, which generates thermoelastic waves to be detected at the cochlea of the inner ear. Experimental and theoretical studies have shown the plausibility of this hypothesis [2], [9]. Consequently, it is now recognized as an established nonthermal biological effect. This phenomenon has been adopted as the basis for limiting exposure to pulsed microwaves in the human safety guidelines [14], [15].

However, those theoretical studies have assumed simplified head models such as a homogeneous sphere. In addition to this simplification, a symmetrical pattern of a specific absorption rate (SAR) was assumed to calculate the thermoelastic waves generated in the sphere model so that the analytical solution could be found [5], [6], [12]. A human head has an anatomically complex structure in shape and in heterogeneity of tissues. It has been shown that the complex shape and dielectric heterogeneity of the human head significantly affect the SAR distribution in the human head exposed to microwaves [16], [17]. Moreover, the heterogeneity of mechanical properties should also affect the elastic waves in the tissue. These considerations motivated us to make numerical studies on the microwave hearing effect, assuming realistic head models taking the anatomical heterogeneity into account.

In this paper, we calculate the thermoelastic waves in a human head with realistic shape and heterogeneity in dielectric and mechanical properties of tissues. These calculations are accomplished by the numerical method of finite-difference time-domain (FDTD) calculation both on the electromagnetic and elastic waves. The effects of the realistic properties of the human head on the generated elastic waves are discussed by comparing the obtained results with the previously reported analytical results. The discussion on the safety of microwave hearing effect with respect to the strength of elastic waves are updated based on the numerical results obtained in this paper.

Manuscript received November 14, 1999; revised May 31, 2000. This work was supported in part by the Ministry of Education, Science, Sports, and Culture, Japan, under a Grant-in-Aid for Scientific Research.

Y. Watanabe, T. Tanaka and M. Taki are with the Department of Electrical Engineering, Tokyo Metropolitan University, Tokyo 192-0397, Japan.

S. Watanabe is with the Communications Research Laboratory, Ministry of Posts and Telecommunications, Tokyo 184-8795, Japan.

Publisher Item Identifier S 0018-9480(00)09706-4.

II. Method of Analysis

We decomposed the analysis into two steps of FDTD calculations to compute thermoelastic waves generated by pulsed microwaves. As the first step, we calculate the SAR distributions based on Maxwell's equation. The SAR produces temperature rise, whose thermal energy exerts stress in the tissues. As the second step, we calculate the thermoelastic waves generated by the thermal stress based on the elastic-wave equation in lossless media. We assume in this analysis that the duration of the incident microwave pulse is much smaller than the time constants of heat conduction and convection in the tissues, so that the temperature rise takes place adiabatically [5]. Although propagating elastic waves may cause temperature change due to mechanical deformation of elastic media, we assume that this effect can be ignored.

A. Numerical Models of the Head

Two different anatomically based models of a human head were used in our study. The first model (i.e., Model 1) is a magnetic resonance imaging (MRI)-based head model for the commercial software X-FDTD provided by REMCOM Inc., State College, PA, which has a resolution of $3 \times 3 \times 3$ mm^3 and consists of bone, brain, cartilage, eye, muscle, and skin. The second model (i.e., Model 2) is another anatomically based head model based on an anatomical chart of a Japanese male, which has a resolution of $2.5 \times 2.5 \times 2.5$ mm^3 and consists of bone, brain, muscle, eye, fat, lens, and skin [18]. Figs. 1 and 2 show the cross sections of these models. To reduce numerical dispersion, we converted the resolution of these models from 3 to 1.5 mm and 2.5 to 1.25 mm, respectively.

Fig. 1. Shape and cross sections of Model 1.

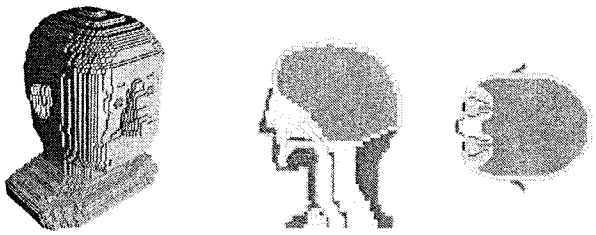

Fig. 2. Shape and cross sections of Model 2.

TABLE I
RESOLUTION OF HEAD MODELS

	cell size	modeled space
Model 1	1.5 mm	306 × 236 × 240
Model 2	1.25 mm	200 × 200 × 210
Sphere model	1.75 mm	80 × 80 × 80

TABLE II
DIELECTRIC PROPERTIES OF THE TISSUES AT 915 MHz [19]

tissue	ε_r	σ [S/m]
bone	16.6	0.244
brain	45.7	0.772
cartilage	42.6	0.789
muscle	55.9	0.975
eye ball	68.9	1.64
fat	11.3	0.110
skin	46.0	0.850
lens	35.8	0.489

In addition to the anatomically based models, we used a 7-cm-radius homogeneous sphere model, which has the known analytical solutions of thermoelastic waves for certain symmetrical SAR distributions [5], [6], [12]. The analytical solutions allow comparison with the numerical results. Table I summarizes the specifications of these models.

B. Calculation of the SAR

The SAR is given by

$$\mathrm{SAR} = \frac{\sigma E^2}{2\rho} \tag{1}$$

where E is the amplitude of electric field, σ is the conductivity, and ρ is the mass density of the tissue. Table II gives the dielectric properties of each tissue.

An E-polarized electromagnetic plane wave is assumed to incident on the back of the head models. The frequency of the microwave is 915 MHz and the incident power density is 1 mW/cm^2.

We calculated the SAR distributions by using the FDTD method for Maxwell's equation [20]. The computational space was truncated by a perfectly matched layer (PML) [21] to minimize unnecessary reflection. We used an eight-cell PML with a parabolic conductivity profile. The theoretical reflection coefficient at normal incidence is -100 dB.

C. FDTD Method for Elastic Waves

We used the FDTD method for elastic waves to compute thermoelastic waves generated by the calculated SAR distributions. The FDTD formulation for elastic waves is derived by descretizing the following equations.

First is the Hooke's law with the thermal stress term

$$\frac{\partial \sigma_{xx}}{\partial t} = (\lambda+2\mu)\frac{\partial v_x}{\partial x} + \lambda\frac{\partial v_y}{\partial y} + \lambda\frac{\partial v_z}{\partial z} - \alpha(3\lambda+2\mu)\frac{\partial T}{\partial t} \tag{2}$$

$$\frac{\partial \sigma_{yy}}{\partial t} = \lambda\frac{\partial v_x}{\partial x} + (\lambda+2\mu)\frac{\partial v_y}{\partial y} + \lambda\frac{\partial v_z}{\partial z} - \alpha(3\lambda+2\mu)\frac{\partial T}{\partial t} \tag{3}$$

$$\frac{\partial \sigma_{zz}}{\partial t} = \lambda\frac{\partial v_x}{\partial x} + \lambda\frac{\partial v_y}{\partial y} + (\lambda+2\mu)\frac{\partial v_z}{\partial z} - \alpha(3\lambda+2\mu)\frac{\partial T}{\partial t} \tag{4}$$

$$\frac{\partial \sigma_{xy}}{\partial t} = \mu\left(\frac{\partial v_x}{\partial y} + \frac{\partial v_y}{\partial x}\right) \tag{5}$$

$$\frac{\partial \sigma_{yz}}{\partial t} = \mu\left(\frac{\partial v_y}{\partial z} + \frac{\partial v_z}{\partial y}\right) \tag{6}$$

$$\frac{\partial \sigma_{zx}}{\partial t} = \mu\left(\frac{\partial v_z}{\partial x} + \frac{\partial v_x}{\partial z}\right) \tag{7}$$

and the second is the equations of motion

$$\rho\frac{\partial v_x}{\partial t} = \frac{\partial \sigma_{xx}}{\partial x} + \frac{\partial \sigma_{xy}}{\partial y} + \frac{\partial \sigma_{zx}}{\partial z} \tag{8}$$

$$\rho\frac{\partial v_y}{\partial t} = \frac{\partial \sigma_{xy}}{\partial x} + \frac{\partial \sigma_{yy}}{\partial y} + \frac{\partial \sigma_{yz}}{\partial z} \tag{9}$$

$$\rho\frac{\partial v_z}{\partial t} = \frac{\partial \sigma_{zx}}{\partial x} + \frac{\partial \sigma_{yz}}{\partial y} + \frac{\partial \sigma_{zz}}{\partial z} \tag{10}$$

where (σ_{ij}) is the stress tensor, v_i is the particle velocity, λ and μ are the Lamé's constants, α is the coefficient of linear thermal expansion, and ρ is the mass density of the tissue.

We assume that the temperature rise T is given by

$$T(x,y,z,t) = \begin{cases} \dfrac{\mathrm{SAR}(x,y,z)}{C_h(x,y,z)}t, & 0 \le t \le t_0 \\ \dfrac{\mathrm{SAR}(x,y,z)}{C_h(x,y,z)}t_0, & t > t_0 \end{cases} \tag{11}$$

where $C_h(x,y,z)$ is the specific heat of the tissue at the point (x,y,z) and t_0 is the pulse duration. These two sets of governing equations are discretized to the FDTD form. Following Yee's notation [20], a point in a Cartesian grid is expressed as

$$(i,j,k) \equiv (i\Delta x, j\Delta y, k\Delta z) \tag{12}$$

and any field value F of discrete space and time is expressed as

$$F^n(i,j,k) \equiv F(i\Delta x, j\Delta y, k\Delta z, n\Delta t) \tag{13}$$

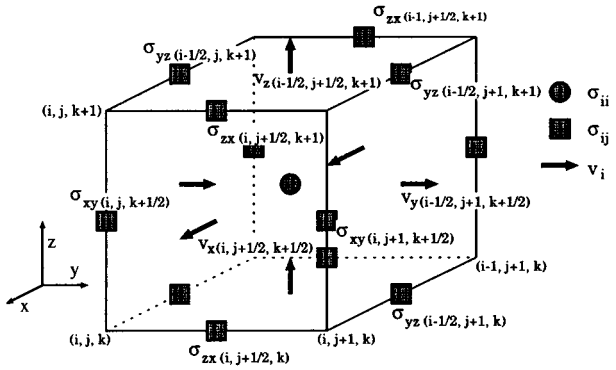

Fig. 3. Staggered cell geometry for elastic-wave computation.

where Δt is time increment, and i, j, k, n are integers. The staggered cell for the FDTD method for elastic waves is shown in Fig. 3.

The field equations are discretized using Yee's leapfrog scheme with centered finite difference, and then the update equations are obtained. For example, from (2), (5), and (8) we have

$$\begin{aligned}
&\sigma_{xx}^{n}\left(i+\frac{1}{2},j+\frac{1}{2},k+\frac{1}{2}\right)\\
&\quad=\sigma_{xx}^{n-1}\left(i+\frac{1}{2},j+\frac{1}{2},k+\frac{1}{2}\right)\\
&\qquad+\frac{(\lambda+2\mu)\Delta t}{\Delta x}\left[v_x^{n-(1/2)}\left(i+1,j+\frac{1}{2},k+\frac{1}{2}\right)\right.\\
&\qquad\qquad\left.-v_x^{n-(1/2)}\left(i,j+\frac{1}{2},k+\frac{1}{2}\right)\right]\\
&\qquad+\frac{\lambda\Delta t}{\Delta y}\left[v_y^{n-(1/2)}\left(i+\frac{1}{2},j+1,k+\frac{1}{2}\right)\right.\\
&\qquad\qquad\left.-v_y^{n-(1/2)}\left(i+\frac{1}{2},j,k+\frac{1}{2}\right)\right]\\
&\qquad+\frac{\lambda\Delta t}{\Delta z}\left[v_z^{n-(1/2)}\left(i+\frac{1}{2},j+\frac{1}{2},k+1\right)\right.\\
&\qquad\qquad\left.-v_z^{n-(1/2)}\left(i+\frac{1}{2},j+\frac{1}{2},k\right)\right]\\
&\qquad-\alpha(3\lambda+2\mu)\Delta t\frac{\partial T\left(i+\frac{1}{2},j+\frac{1}{2},k+\frac{1}{2}\right)}{\partial t}
\end{aligned}\tag{14}$$

$$\begin{aligned}
&\sigma_{xy}^{n}\left(i,j,k+\frac{1}{2}\right)\\
&\quad=\sigma_{xy}^{n-1}\left(i,j,k+\frac{1}{2}\right)\\
&\qquad+\frac{\mu\Delta t}{\Delta x}\left[v_y^{n-(1/2)}\left(i+\frac{1}{2},j,k+\frac{1}{2}\right)\right.\\
&\qquad\qquad\left.-v_y^{n-(1/2)}\left(i-\frac{1}{2},j,k+\frac{1}{2}\right)\right]\\
&\qquad+\frac{\mu\Delta t}{\Delta y}\left[v_x^{n-(1/2)}\left(i,j+\frac{1}{2},k+\frac{1}{2}\right)\right.\\
&\qquad\qquad\left.-v_x^{n-(1/2)}\left(i,j-\frac{1}{2},k+\frac{1}{2}\right)\right]
\end{aligned}\tag{15}$$

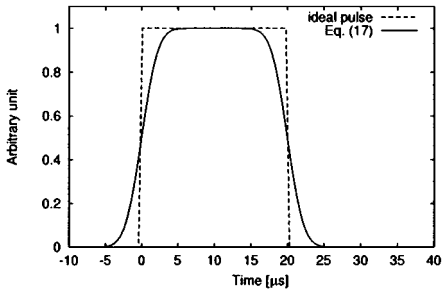

Fig. 4. Shape of (17) for 20-μs pulse used in the FDTD calculation.

$$\begin{aligned}
&v_x^{n+(1/2)}\left(i,j+\frac{1}{2},k+\frac{1}{2}\right)\\
&\quad=v_x^{n-(1/2)}\left(i,j+\frac{1}{2},k+\frac{1}{2}\right)\\
&\qquad+\frac{\Delta t}{\rho\Delta x}\left[\sigma_{xx}^{n}\left(i+\frac{1}{2},j+\frac{1}{2},k+\frac{1}{2}\right)\right.\\
&\qquad\qquad\left.-\sigma_{xx}^{n}\left(i-\frac{1}{2},j+\frac{1}{2},k+\frac{1}{2}\right)\right]\\
&\qquad+\frac{\Delta t}{\rho\Delta y}\left[\sigma_{xy}^{n}\left(i,j+1,k+\frac{1}{2}\right)-\sigma_{xy}^{n}\left(i,j,k+\frac{1}{2}\right)\right]\\
&\qquad+\frac{\Delta t}{\rho\Delta z}\left[\sigma_{zx}^{n}\left(i,j+\frac{1}{2},k+1\right)-\sigma_{zx}^{n}\left(i,j+\frac{1}{2},k\right)\right].
\end{aligned}\tag{16}$$

The source term $\partial T/\partial t$ should be derived from (11). Instead of simply taking a time derivative of (11), we used the following functional form for this term in order to reduce higher frequency components that cannot be efficiently computed by the finite-difference method:

$$\frac{\partial T(x,y,z,t)}{\partial t}=\frac{\mathrm{SAR}(x,y,z)}{2C_h(x,y,z)}\Big\{\mathrm{erf}(at)-\mathrm{erf}\big(a(t-t_0)\big)\Big\}.\tag{17}$$

The parameter a in (17) represents the steepness of the microwave pulse. We assumed $a=0.4\times10^6$ in the following analysis (Fig. 4). In a similar way, the corresponding equations for updating other field values can be obtained by discretizing (3), (4), (6), (7), (9), and (10).

In these calculations, the stress-free condition $\sigma_{ij}^{n}\equiv 0$ was applied as the boundary condition at the surface of the models. As it may not be realistic to assume the stress-free condition on the bottom of the head models, we employed the PML absorbing boundary on those boundaries. We used a ten-cell PML with a parabolic profile of a stretching coefficient of attenuation [22]. The theoretical reflection coefficient at normal incidence is -60 dB for the p wave.

Table III gives elastic and thermal properties assumed in our simulation. Lin [5] assumed the coefficient of the thermal expansion of soft tissue to be 60% of the corresponding value for water. We assumed the same value for the soft tissues. We used the coefficient of thermal expansion of dentine [23] for that of bone.

TABLE III
ELASTIC PROPERTIES OF THE TISSUES [5], [23]–[25]

		soft tissues	bone
density: ρ	[kg/m^3]	1050	1700
specific heat: C_h	[J/kg ℃]	3860	1600
Lamé's constant: λ	[GPa]	2.240	6.923
Lamé's constant: μ	[GPa]	1.052×10^{-6}	4.615
coefficient of thermal expansion : α	[1/℃]	4.1×10^{-5}	1.06×10^{-5}

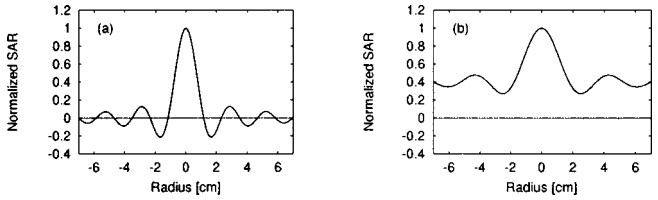

Fig. 5. Normalized symmetrical SAR distributions. (a) Assumed by [5], [6]. (b) Assumed by [12].

III. SPHERE MODEL

A. Thermoelastic Waves for Approximated SAR Distributions

Lin [5], [6] and Shibata [12] have derived analytical solutions of thermoelastic waves generated in a sphere exposed to a plane microwave pulse assuming that the SAR distributions could be approximated by spherically symmetric functions. Lin [5] assumed the SAR distribution at 918 MHz for a brain-equivalent sphere given by

$$\frac{I_0}{\rho}\,\frac{\sin(6\pi r/r_0)}{6\pi r/r_0} \tag{18}$$

where I_0 is the peak absorbed energy, r is the radial variable, and r_0 is the radius of the sphere, which equals 7 cm simulating an adult human head. Shibata [12] considered surface heating, and assumed the SAR distribution given by

$$\frac{I_0}{\rho}\left(0.4+0.6\frac{\sin(4\pi r/r_0)}{4\pi r/r_0}\right). \tag{19}$$

These SAR distributions are shown in Fig. 5.

In order to verify the accuracy of the FDTD method for elastic waves, we compared the pressure waves calculated by the FDTD method with the analytical solutions of pressure waves in a sphere assuming the same SAR distributions as they used. The pressure p is defined as follows:

$$p=\frac{1}{3}\sum_{i=x,y,z}\sigma_{ii}. \tag{20}$$

Figs. 6 and 7 show comparison of the FDTD results and the analytical solutions of pressure waves at the center of the sphere. The incident power density was 1 mW/cm^2 and pulse duration was 20 μs. The results agreed well, which confirmed validity of our FDTD coding.

B. Thermoelastic Waves for the Exact SAR Distribution

Thermoelastic waves are computed by the FDTD method using the exact SAR distribution calculated by the Mie series solution [26] (Fig. 8). Fig. 9 shows the calculated pressure waveform at the center of the sphere.

Compared with Figs. 6 and 7, the waveform for the exact SAR distribution is similar to Fig. 7 rather than Fig. 6. This result suggests that the surface heating is important in generating elastic

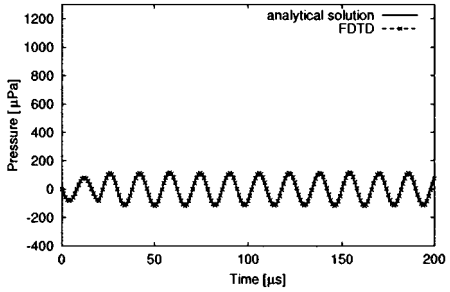

Fig. 6. Comparison of the pressure waveforms of the analytical solution and of the FDTD result at the center of the sphere with the SAR distribution shown in Fig. 5(a).

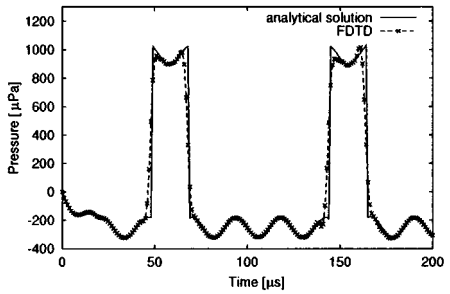

Fig. 7. Comparison of the pressure waveforms of the analytical solution and of the FDTD result at the center of the sphere with the SAR distribution shown in Fig. 5(b).

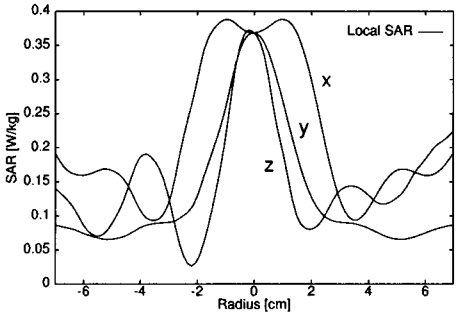

Fig. 8. SAR distribution in a sphere along the three Cartesian coordinates at 1 mW/cm^2 of incident power density obtained by the exact analytical solution of Mie series.

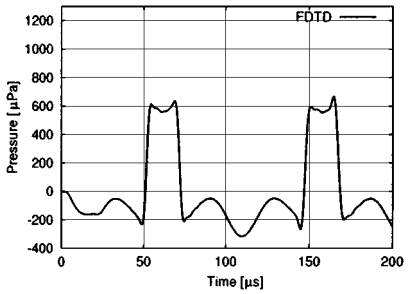

Fig. 9. Pressure waveform at the center of the sphere calculated by FDTD method assuming the exact SAR distribution shown in Fig. 8.

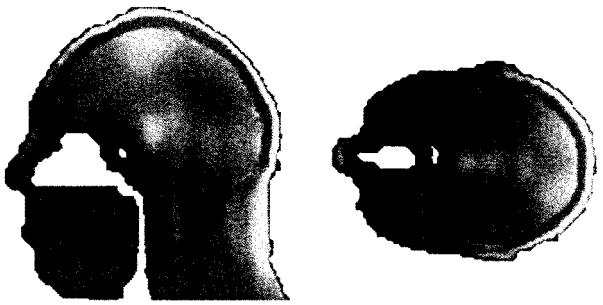

Fig. 10. SAR distribution in Model 1 exposed to 915-MHz plane waves, which are incident on the back of the head.

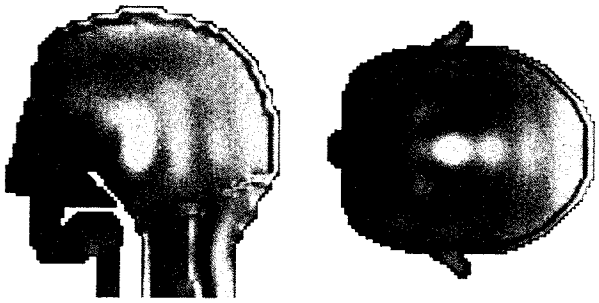

Fig. 11. SAR distribution in Model 2 exposed to 915-MHz plane waves, which are incident on the back of the head.

waves. That is, surface heating excites the fundamental mode of the elastic waves, while the SAR distribution without surface heating mainly excites higher modes.

IV. Human Head Models

Figs. 10 and 11 show the calculated SAR distributions at 915 MHz for the anatomically based models. The peak 1-g averaged SARs for 1 mW/cm^2 are 0.30 and 0.34 W/kg for Model 1 and 2, respectively.

We calculated thermoelastic waves generated in human tissue from these SAR distributions. Figs. 12 and 13 show the pressure waveform at the cochlea of the anatomically based models generated by a single pulse with 20-μs duration. The waveforms are much more complex than those of the sphere model (Fig. 9). The difference should be attributed to the complex shape and heterogeneity of the head models. Fig. 14 shows power spectra of the pressure waves. The dominant frequency components lie in 7–9 kHz. These peaks correspond to the resonant frequencies of pressure waves in the head. Figs. 15 and 16 show the sequence of the distribution of pressure waves in a cross section of the head. These figures show that the wavefront is initiated in the back of the head, where the large SAR appears, focuses on the center, and then reverberates many times.

The calculated values of peak pressure at the cochlea and the maximum peak pressure within the head models are shown in Table IV. The largest pressure appeared near the center of the head in the anatomically based models as well as in the sphere model. The maximum peak values were of the same order.

We compared the amplitude of the calculated pressure with bone conduction hearing, as Lin did [5]. The threshold for bone conduction hearing was reported to be about 60 dB (Re 20 μPa) or 20 000 μPa at frequencies of 5–10 kHz [27]. The

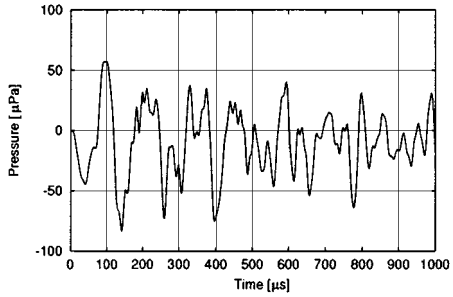

Fig. 12. Pressure waveform at the cochlea of Model 1 exposed to a single 20-μs pulse at 915 MHz, 1 mW/cm^2.

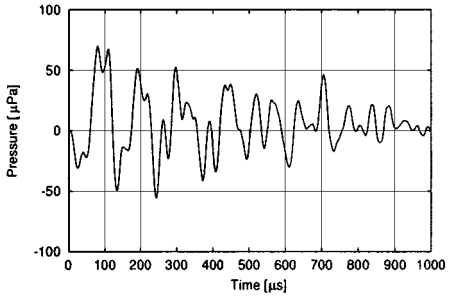

Fig. 13. Pressure waveform at the cochlea of Model 2 exposed to a single 20-μs pulse at 915 MHz, 1 mW/cm^2.

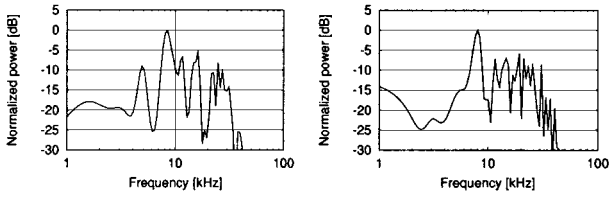

(a) (b)

Fig. 14. Power spectra of the elastic waves at the cochlea. (a) Model 1. (b) Model 2.

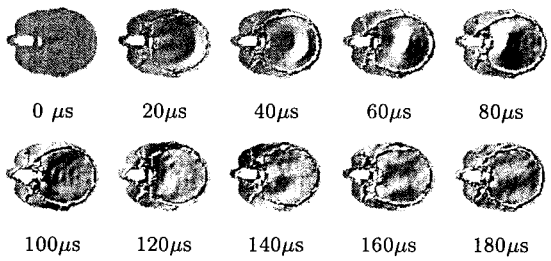

Fig. 15. Sequence of the distribution of pressure waves in Model 1.

TABLE IV
Calculated Values of Peak Pressure

model	cochlea	whole head
Model 1	83 μPa	270 μPa
Model 2	70 μPa	590 μPa
Sphere model	-	670 μPa
Sphere model†	-	120 μPa
Sphere model‡	-	1000 μPa

†‡calculated by analytical solution given in [5], [12] respectively.

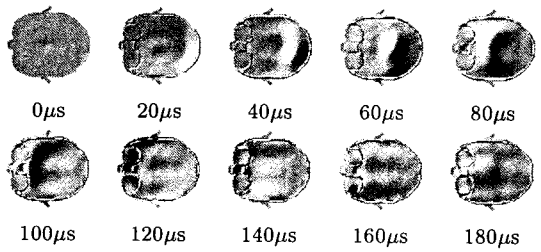

Fig. 16. Sequence of the distribution of pressure waves in Model 2.

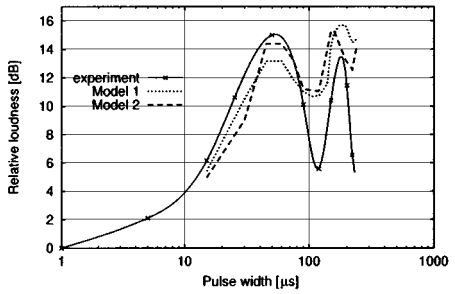

Fig. 17. Pulsewidth dependencies of the calculated peak pressures and the perceived loudness obtained experimentally. The experimental data is from [7], which was given in [13].

TABLE V
COMPARISON OF THE STRENGTH OF MICROWAVE-INDUCED SOUND AT THRESHOLD OF PERCEPTION AND ULTRASOUND USED IN MEDICAL DIAGNOSIS

	MW-induced sound	diagnostic ultrasound
peak pressure	0.18 Pa†	7700 Pa
power density	1.0×10^{-9} mW/cm^2	2 mW/cm^2
displacement	0.0023 nm	0.33 nm

†peak pressure at the cochlea is 0.02 Pa.

calculated peak pressures at the cochlea are 83 and 70 μPa in Model 1 and Model 2, respectively, for 1-mW/cm^2 incident power density and 20-μs pulsewidth. Hence, the power density of 300 mW/cm^2 is required to make the same order of the peak pressure as the threshold of bone conduction hearing. This magnitude of power density is near the reported threshold of microwave hearing [8].

Diagnostic ultrasound generally ranges from 2 to 500 mW/cm^2 in spatial peak temporal average (SPTA) value [28]. A comparison is given in Table V between the strengths of microwave-induced pressure at the perception threshold and the ultrasound for medical diagnosis. We assume here a plane wave at 2.5 MHz for diagnostic ultrasound. The microwave-induced pressure is far smaller than ultrasound for medical diagnosis. We should note that the spatial peak temporal power (SPTP) of diagnostic ultrasound is much higher than the value in Table V. Hence, it is suggested that microwave hearing effect at the threshold level is not likely to be hazardous with regard to the strength of the pressure waves.

It has been reported that the loudness of microwave hearing depends on the pulse duration [1], [7]. Fig. 17 shows the calculated peak sound pressures at the cochlea in the head models as a function of pulsewidth. It also shows the experimental result of perceived loudness as a function of pulsewidth obtained by Tyazhelov [7]. These characteristics are similar to each other. The peak sound pressure or the loudness increases as pulsewidth increases from 5 to 50 μs, then diminishes with further increase of pulsewidth from 70 to 100 μs, and then increases again with longer pulsewidth.

The resonance frequency of pressure waves in the head has been shown to be 7–9 kHz in our analysis. A microwave pulse with duration of a half-cycle of the resonant frequency, i.e., about 50 μs, most efficiently excites thermoelastic waves because the thermal stress energy is fully integrated into thermoelastic waves. If the pulse duration is longer than this, phase cancellation of elastic waves occurs. When the pulse duration is one cycle of the resonance frequency, the phase cancellation is most remarkable and the elastic waves are not excited efficiently. The oscillating characteristics seen in Fig. 17 are clearly explained through the numerical results obtained in this paper.

V. CONCLUSION

Numerical studies on the microwave hearing effect have been presented in this paper. We derived the formulation to update the field variables in the elastic-wave equations with thermal stress by the FDTD method. The validity of the FDTD analysis for elastic waves was confirmed through comparison of the numerical results with the analytical solutions in a sphere model.

The elastic waves excited by microwave pulses were numerically calculated by the FDTD method developed in this paper. Two anatomically based head models were employed. The waveforms of calculated pressure waves were different from the previously reported ones. It was especially shown that the surface heating was important in exciting the fundamental mode of the pressure waves in the head. The waveforms at the cochlea of realistic head models were much more complex than that in a sphere model. The resonant frequencies in the head were estimated to be 7–9 kHz. The pulsewidth dependency of loudness of microwave hearing was explained by the simulations with realistic head models.

The strength of the pressure waves was evaluated to consider the safety of this phenomenon. The peak pressure of elastic waves in the realistic head models were of the same order as the previously reported values obtained with a homogeneous sphere model assuming a symmetrical SAR distribution. The peak pressure, power density, and displacement of this phenomenon were much less than the average values of those quantities of ultrasound used in medical diagnosis. It was suggested that microwave hearing is not likely to be hazardous with regard to the strength of pressure waves.

However, further studies will be necessary to establish the safety of this effect. Although Lin [4] showed that thermoelastic stress was dominant over strictive force and radiation pressure based on the calculation with the homogeneous model, we cannot conclude that it is also true in an actual human head, which is highly heterogeneous. Direct interaction of high peak electric field with tissue also cannot be excluded. The numerical analysis of elastic waves in a heterogeneous structure presented in this paper will contribute to further studies on the interaction between pulsed electromagnetic fields and biological bodies.

REFERENCES

[1] A. H. Frey and R. Messenger, Jr., "Human perception of illumination with pulsed ultra-high frequency electromagnetic energy," *Science*, vol. 181, pp. 356–358, 1973.

[2] K. R. Foster and E. D. Finch, "Microwave hearing: Evidence for thermoacoustic auditory stimulation by pulsed microwaves," *Science*, vol. 185, pp. 256–258, 1974.

[3] C. K. Chou, R. Galambos, A. W. Guy, and R. H. Lovely, "Cochlea microphonics generated by microwave pulses," *J. Microwave Power*, vol. 10, pp. 361–367, 1975.

[4] J. C. Lin, "Microwave auditory effect—A comparison of some possible transduction mechanisms," *J. Microwave Power*, vol. 11, pp. 77–81, 1976.

[5] ——, "On microwave-induced hearing sensation," *IEEE Trans. Microwave Theory Tech.*, vol. MTT-25, pp. 605–613, July 1977.

[6] ——, "Further studies on the microwave auditory effect," *IEEE Trans. Microwave Theory Tech.*, vol. MTT-25, pp. 939–943, July 1977.

[7] V. V. Tyazhelov, R. E. Tigranian, E. O. Khizhniak, and I. G. Akoev, "Some peculiarities of auditory sensations evoked by pulsed microwave fields," *Radio Sci.*, vol. 14, no. 6S, pp. 259–263, 1977.

[8] J. C. Lin, "Microwave auditory phenomenon," *Proc. IEEE*, vol. 68, pp. 67–68, Jan. 1980.

[9] R. G. Olsen and J. C. Lin, "Microwave pulse-induced resonances in spherical head models," *IEEE Trans. Microwave Theory Tech.*, vol. MTT-29, pp. 1114–1117, Oct. 1981.

[10] C. K. Chou and A. W. Guy, "Auditory perception of radio-frequency electromagnetic fields," *J. Acoust. Soc. Amer.*, vol. 71, pp. 1321–1334, 1982.

[11] R. G. Olsen and J. C. Lin, "Microwave-induced pressure waves in mammalian brains," *IEEE Trans. Biomed. Eng.*, vol. BME-30, pp. 289–294, May 1983.

[12] T. Shibata, O. Fujiwara, K. Kato, and T. Azakami, "Calculation of thermal stress inside human head by pulsed microwave irradiation" (in Japanese), *IEICE Trans. Commun.*, vol. J69-B, no. 10, pp. 1144–1146, 1986.

[13] J. C. Lin, "Auditory perception of pulsed microwave radiation," in *Biological Effects and Medical Applications of Electromagnetic Energy*, O. P. Gandhi, Ed. Englewood Cliffs, NJ: Prentice-Hall, 1990, pp. 277–318.

[14] ICNIRP, "Guidelines for limiting exposure to time-varying elestric, magnetic, and electromagnetic fields (up to 300 GHz)," *Health Phys.*, vol. 74, no. 4, pp. 494–522, 1998.

[15] *IEEE Standard for Safety Levels with Respect to Human Exposure to Radio Frequency Electromagnetic Fields 3 kHz to 300 GHz*, ANSI/IEEE Standard C95.1-1992, 1992.

[16] S. Watanabe, M. Taki, T. Nojima, and O. Fujiwara, "Characteristics of the SAR distributions in a head exposed to electromagnetic fields radiated by a hand-held portable radio," *IEEE Trans. Microwave Theory Tech.*, vol. 44, pp. 1874–1883, Oct. 1996.

[17] O. P. Gandhi, G. Lazzi, and C. M. Furse, "Electromagnetic absorption in the human head and neck for mobile telephones at 835 and 1900 MHz," *IEEE Trans. Microwave Theory Tech.*, vol. 44, pp. 1884–1897, Oct. 1996.

[18] O. Fujiwara and A. Kato, "Computation of SAR inside eyeball for 1.5-GHz microwave exposure using finite-difference time-domain technique," *IEICE Trans. Commun.*, vol. E77-B, pp. 732–737, 1994.

[19] C. Gabriel, "Compilation of the dielectric properties of body tissues at RF and microwave frequencies," Armstrong Laboratory, Brooks Air Force Base, Brooks AFB, TX, Tech. Rep. AL/OE-TR-1996-0037, 1998.

[20] L. Kunz, *The Finite Difference Time Domain Method for Electromagnetics*. Boca Raton, FL: CRC Press, 1993.

[21] J.-P. Berenger, "A perfectly matched layer for the absorption of electromagnetic waves," *J. Comput. Phys.*, vol. 114, no. 1, pp. 185–200, 1994.

[22] W. C. Chew and Q. H. Liu, "Perfectly matched layers for elastrodynamics: A new absorbing boundary condition," *J. Comput. Acoust.*, vol. 4, no. 4, pp. 341–359, 1996.

[23] D. N. Fenner, P. B. Robinson, and P. M.-Y. Cheung, "Three-dimensional finite element analysis of thermal shock in a premolar with a composite resin MOD restoration," *Med. Eng. Phys.*, vol. 20, pp. 269–275, 1998.

[24] V. K. Goel, H. Park, and W. Kong, "Investigation of vibration characteristics of the ligamentous lumber spine using the finite element approach," *ASME J. Biomech. Eng.*, vol. 116, pp. 337–383, 1994.

[25] R. G. Gordon, R. B. Roemer, and S. M. Horvath, "A mathematical model of the human temperature regulatory system—Transient cold exposure response," *IEEE Trans. Biomed. Eng.*, vol. BME-23, pp. 434–444, Nov. 1976.

[26] J. A. Stratton, *Electromagnetics Theory*. New York: McGraw-Hill, 1941.

[27] J. F. Corso, "Bone-conduction thresholds for sonic and ultrasonic frequencies," *J. Acoust. Soc. Amer.*, vol. 35, no. 11, pp. 1738–1743, Nov. 1963.

[28] R. L. Powis and W. J. Powis, "Bioeffects of ultrasound on tissue," in *A Thinker's Guide to Ultrasonic Imaging*. Baltimore, MD: Urban & Schwarzenberg, 1984, pp. 239–253.

Yoshiaki Watanabe received the B.E. degree in electrical engineering from the Tokyo Metropolitan University, Tokyo, Japan, in 1999, and is currently working toward the M.E. degree in electrical engineering at the Tokyo Metropolitan University.

His research interests include digital signal processing and numerical simulation of electromagnetic and acoustic waves.

Toshiyuki Tanaka (M'89) received the B.E., M.E., and D.E. degrees in electronic engineering from the University of Tokyo, Japan, in 1988, 1990, and 1993, respectively.

He is currently a Lecturer in the Department of Electrical Engineering, Graduate School of Engineering, Tokyo Metropolitan University, Tokyo, Japan. He has been engaged mainly in research on theoretical studies of neural networks.

Masao Taki was born in Tokyo, Japan, in 1953. He received the B.E. degree and the M.E. and Ph.D. degrees in electronic engineering from the University of Tokyo, Tokyo, Japan, in 1976, 1978, and 1981, respectively.

He is currently a Professor in the Department of Electrical Engineering, Graduate School of Engineering, Tokyo Metropolitan University, where he has been engaged in research on biological effects of electromagnetic fields and noise-control engineering.

Dr. Taki is a member of the Institute of Electronics, Information and Communication Engineers (IEICE), Japan, the Japan Society of Medical and Biological Engineering, and the Acoustical Society of Japan.

So-ichi Watanabe (S'94–M'96) received the B. E., M. E., and Ph. D. degrees in electrical engineering from the Tokyo Metropolitan University, Tokyo, Japan, in 1991, 1993, and 1996, respectively.

He is currently with the Communication Research Laboratory, Ministry of Posts and Telecommunications, Tokyo, Japan. His main interests have been biological effects of electromagnetic fields.

Dr. Watanabe is a member of the Institute of Electronics, Information and Communication Engineers (IEICE), Japan.